Numerical and experimental study for the design of electrocoagulation reactor for dye removal

Claudia Luiza Manfredi Gasparovic[a,*], Eduardo Eyng[a], Laercio Mantovani Frare[a], Fábio Orssatto[a], Marcelo Risso Errera[b]

[a]Graduate Program in Environmental Technologies, Federal University of Technology, Parana, Brasil Avenue, 85804-000, Medianeira, Parana, Brazil, emails: claudiagasparovicea@gmail.com (C.L.M. Gasparovic), eduardoeyng@utfpr.edu.br (E. Eyng), laercio@utfpr.edu.br (L.M. Frare), orssatto@utfpr.edu.br (F. Orssatto)
[b]Department of Environmental Engineering, Federal University of Parana, Av. Francisco H. dos Santos, Centro Politécnico, 81531-980, Curitiba, Parana, Brazil, email: errera@ufpr.br

ABSTRACT

Water resources are increasingly scarcer and more expensive to collect, treat and distribute. Advanced industrial wastewater treatment methods, such as electrocoagulation (EC), have become more viable. However, the design of EC reactors is very complex and costly since it varies significantly with wastewater composition. In order to ease the efforts in design, this paper proposes a novel procedure for the simulation of EC systems, which couples computational fluid dynamics (CFD) with a kinetic model for pollutant removal. A CFD model was calibrated with an experimentally fitted kinetic model for Reactive Blue dye 5G removal from synthetic solution to predict the residual concentration profile in a lab-scale continuous flow reactor. Simulations were carried out with a current density of 8.65 mA·cm^{-2}, initial dye concentrations of 25 and 40 mg·L^{-1}, and flow rates of 0.5–2 L·min^{-1}. Results were compared to experimental data from a 23-point sampling mesh of the reactor. The model successfully predicted the reactor concentration profile for a range of low flow velocities (from 0.5 to 1 L·min^{-1}), presenting a relative error of less than 2% for a dye removal of 87%–98% at the reactor exit. This paper shows that coupling a kinetic model for pollutant removal based on experimental observation with CFD offers reliable information for EC reactor design with a good compromise between time and resources. The use of computational tools with the proposed methodology can aid in designing EC reactors, thus helping to solve a major obstacle to expanding this promising technology.

Keywords: Electroflocculation; Electrocoagulation; Computational fluid dynamics; Kinetics; Dye removal; Textile wastewater treatment

1. Introduction

Water resources are increasingly scarcer, more expensive to collect and distribute, and harder to treat, thus increasing the interest in water reuse, especially from and for industries. The textile industry is notable for its high polluting potential, mainly due to the production of large volumes of liquid effluents [1,2] characterized by the presence of dyes [3,4].

About 7 × 10^5 tons of dye are produced annually worldwide, around 10%–15% of which enters the environment, especially water resources, without any treatment process. This is problematic since these compounds can harm the environment and ecosystems, presenting proven toxicity [5].

Azo dyes are mostly toxic and carcinogenic and cause harm to humans and the environment [6]. They present recalcitrant characteristics that make their removal

challenging, thus motivating the need for innovative approaches to their treatment [7].

Those compounds can affect the quality of receiving water bodies, for they are usually toxic to aquatic species [8,9]. Textile dyes are highly stable and difficult to degrade [7,10]. The treatment of such wastewater, particularly the removal of color from textile effluents before disposal, is one of the main challenges for the industry [11,12]. Among the most used and polluting dyes in the dyeing industry is the Reactive Blue 5G [13].

Therefore, a treatment method for dye effluents that is sustainable and efficient in the long term is required [14]. Often the treatment processes in the textile industry are based on the operation of precipitation-coagulation physical–chemical systems, followed by biological treatment through an activated sludge system [15]. This process has the disadvantage of producing large amounts of sludge, rich in pigments and other textile materials [5]. Other physical–chemical processes include chemical oxidation, chemical precipitation, membrane nanofiltration, ion exchange, and adsorption [16]. Each of these technologies has some advantages and disadvantages [17], for they are generally expensive (i.e., membrane processes) and often present operational issues [8,18], such as subpar efficiency and high demands on time, energy, and operational space [19]. Often they also incur the production of secondary pollution, as in oxidation–reduction processes [20]. Therefore, the need for more efficient and less expensive ways to remove dyes from effluents encourages research for new treatment technologies, and advanced industrial wastewater treatment methods, such as electrocoagulation (EC), have become more viable [16].

Electrocoagulation has been proven in literature as a promising water treatment technology [21], presenting high efficiency in color removal and the treatment of complex effluents, such as those of the textile industry [22]. Therefore, several studies have employed electrocoagulation for treating textile wastewater, achieving over 90% of dye removal efficiency [22–30]. Among the advantages of this technology are its ease of operation, inexpensiveness and lower sludge generation [31], a higher surface area of the produced flakes plus the fact that it does not require the addition of chemicals [32], environmental compatibility, and versatile nature [19].

Electrocoagulation is based on the *in-situ* generation of coagulant ions by the dissolution of a sacrificial metal anode and the simultaneous production of gaseous hydrogen at the cathode [32]. The coagulant ions formed allow the removal of pollutants by destabilizing contaminant particles present in the effluent through the main mechanisms of neutralization of charges and sweep coagulation [21,33] as well as through the formation of flocks, which float to the surface due to the gas bubbles also resulting from the process [34].

Since EC requires electricity which can present high costs, it needs to be carried out in the most favorable conditions, especially when in the presence of organic matter (as is the case of textile wastewaters), which hinders the EC ability to remove heavy metals [35]. The design of electrocoagulation (EC) reactors is very complex since it varies greatly with the wastewater composition and the target pollutants for removal. Literature points to a lack of technical knowledge and systematic methodologies for designing and dimensioning reactors, especially ones with continuous flow, as some of the main obstacles to the expansion of the technology. Most studies address only batch systems [32,36–38] with limited industrial applications.

The modeling of electrocoagulation processes can significantly aid the design and reduce operational and equipment costs by allowing the study of possible operating conditions and better reactor designs [37,39]. Several approaches to modeling and simulation in literature seek to solve this problem.

Overall, the literature on EC modeling has been focused on either experimental relations for its target function (pollutant removal) [40–42] or theoretical models for its auxiliary phenomena (hydrodynamics and electrochemical). Most of these studies focus on each of the individual phenomena that make up the complex electrocoagulation process [37,39], such as the electrochemical reactions, coagulation and flocculation mechanisms, bubble generation, pH influence, mixing, and electric and velocity field.

Some studies have also been carried out aiming to incorporate several aspects of the process in the model [39,43–45]. Hakizimana et al. [37] point to the so-called computational fluid dynamics (CFD) as one of the most promising approaches to modeling the process; however, they emphasize that it still needs development and the inclusion of more physics. Several works have employed CFD in the study of electrocoagulation reactors, including on current field [46], hydrodynamics [47,48], along with the coupling of both of these phenomena [45,49,50], sometimes with the inclusion of mass transfer for the ions involved [51–54]. With this usual approach, only information regarding flow, current distribution, and coagulant ions can be obtained, which is insufficient for the project. It does not allow, for example, the prediction of a pollutant concentration profile in the electrochemical reactor, which might provide guidelines to define dimensions and operational conditions.

In contrast, few of these works have included the target pollutant concentration in any manner [55], and not ever providing a numerical simulation of the pollutant concentration profile in the reactor. In addition, although some of these works [48,53–55] combine numerical studies with experimental verification of some of the physics, there is a definite lack of papers performing experimental validation on pollutant removal.

Literature review points to a definite gap in modelling approaches that needs to be addressed in order to advance EC applications and scale-up. In sum, pure mathematical models do not provide satisfactory tools for reactor design, nor do empirical methods offer a reliable and systematic tool [41,42,56].

The main innovation of this work is introducing empirical and calibrated kinetic relations for the actual purpose of EC (in this case, dye removal) in a full-scale mathematical model of a working bench-scale reactor prototype to address the main issues that would guide EC reactor design. This study, therefore, coupled CFD to an experimentally fitted kinetic model for the removal of the Reactive Blue dye 5G [57] in an electrocoagulation reactor of continuous flow to predict the concentration profile in the reactor and then validate the model with experimental data.

The model developed in this paper is valid for a range of flow rate conditions and hydraulic retention time (HRT). In addition, the model provided information that would be essential for designing and determining reactor operating conditions.

2. Materials and methods

2.1. Characterization of the electrochemical reactor

The system under study is a continuous flow reactor with multiple parallel plate electrodes in the EC chamber. Its configuration was conceived based on the guidelines described in the literature [58].

The electrodes are arranged to allow a serpentine flow so that the effluent approaches both the cathode and the anode and undergoes multiple polarity changes along the path. This makes a complete treatment possible in a single passage [32].

The electrochemical reactor consists of a tempered glass tank with approximately 14 L and a working volume close to 8.5 L, illustrated in Fig. 1. Four electrode pairs were used, with an effective area of 99 cm² each.

The stock solution was prepared by dissolving pre-defined amounts of dye in distilled water and adding sodium chloride at a concentration of 5 g·L⁻¹ to adjust the conductivity of the solution (7.00 ± 0.56 mS·cm⁻¹). Experimental procedures are further detailed in Gasparovic et al. [57].

The prepared effluent is stored in vessel (a), from where it is pumped to the mixing chamber (b). The effluent then enters the electrolytic chamber (c) containing two deflectors (d/d'), and it flows through the module continuously, passing through four pairs of iron electrodes (e). The electrodes are fed with electric current from bench power supplies (f), with parallel-monopolar type connections (g). The stream exits the reactor and is collected in a second vessel (h).

Each pair of independent current outputs is connected to a pair of electrodes (the positive polarity output to the anode and the negative polarity to the cathode of each pair). Electrode polarity alternates throughout the module, with the first electrode being the cathode, the second the anode, and so on.

2.2. Model and numerical procedure

The numerical model of the electrochemical reactor was developed and solved in COMSOL Multiphysics® Software v.5.2, which uses the finite element method (FEM) to solve the partial differential equations describing the flow field and mass balance of dye.

The geometry used for the simulations was built in COMSOL Multiphysics® Software v.5.2 and is illustrated in Fig. 2. A transparency effect is used to better show the position of the electrodes.

Some modeling assumptions were adopted: density and viscosity of the effluent were considered constant and equal to water's; incompressible fluid; steady-state, single-phase, and laminar flow regime; and a constant temperature of 293.15 K.

The model was validated experimentally by comparing the dye concentration profile predicted by the simulations to experimental data obtained from a 23-point sampling mesh of the reactor, according to procedure described in section 2.3.2.

2.2.1. Fluid dynamics and mass transfer

The flow field was modeled by considering the continuity and Navier–Stokes equations for steady-state incompressible flow [59]:
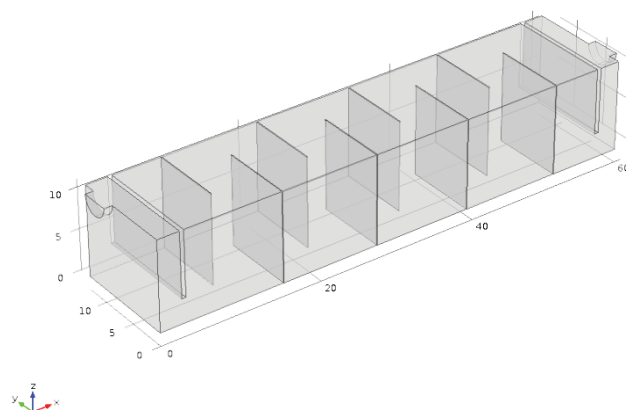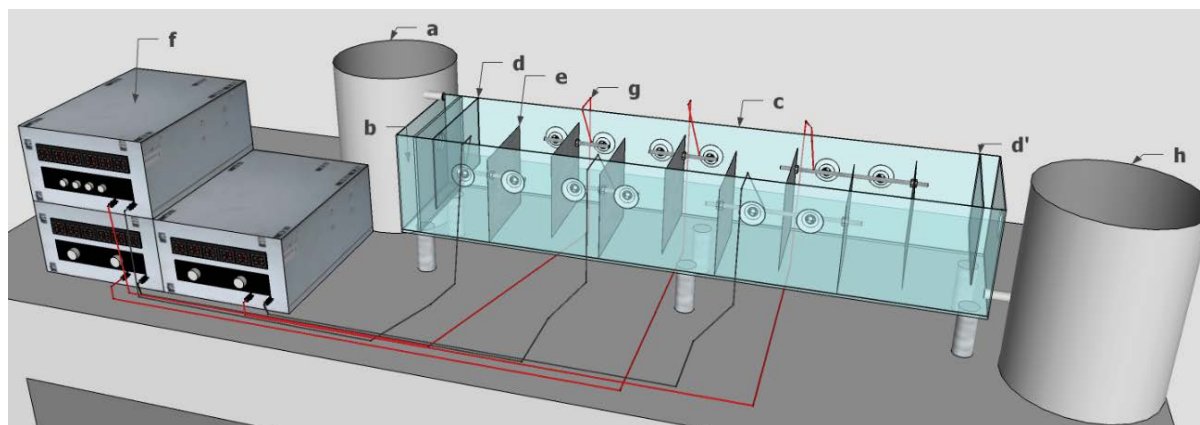

Fig. 2. Geometry of the reactor.

Fig. 1. Schematic representation of the electrocoagulation module, showing (a) affluent vessel, (b) mixing chamber, (c) electrolytic chamber, (d and d') deflectors, (e) electrodes, (f) power supplies, (g) electric connections and (h) effluent vessel.

$$\nabla \cdot \left(\boldsymbol{u} \right) = 0 \tag{1}$$

$$\rho = \rho \boldsymbol{g} - \nabla p + \mu \boldsymbol{u} \tag{2}$$

where $\boldsymbol{u}$ is the fluid velocity field, ρ fluid specific mass, μ fluid viscosity, $\boldsymbol{g}$ is the gravity field, and p is fluid pressure.

Preliminary simulations were performed using laminar flow and turbulent flow interfaces (model k–ε) based on the Navier–Stokes flow equations. Due to a low-velocity profile resulting from both models, the laminar model was chosen as the most likely to accurately predict the flow in the reactor.

The mass balance for the dye species is given by [37]:

$$\frac{DC}{Dt} = D\nabla^2 C + R_i \tag{3}$$

where C is the dye concentration, D is the diffusivity, R_i is the source term (in this case, the reaction rate of dye removal), and D/Dt represents the "material derivative" operator, $D / Dt = \partial / \partial t + \boldsymbol{V} \cdot \nabla$.

As in most CFD studies of electrocoagulation reactors [57], the influence of electrochemical phenomena on the flow and transport of particles, such as the generation of gas bubbles and ion migration, respectively, was ignored. Therefore, a weak coupling was adopted between the physics, in which fluid dynamics affects mass transport, but the opposite does not occur.

2.2.2. Reaction for dye removal

The reaction for dye removal was considered homogeneous and irreversible and assumed to occur in a steady state, where the accumulation of floated sludge in time does not affect the concentration profile. The model used to describe the kinetics was fitted from experimental data as described in a previous work by the authors and describes dye concentration in a batch EC system as a function of time through a sigmoidal logistic curve [60]. For the simulation of the dye removal reaction, the sigmoidal logistic model autonomous function (as described by the authors) was used, according to Eq. (4), for the reaction rate R_i (mol·m^{-3}·s^{-1}):

$$R_i = \frac{dC}{dt} = \left\{ k\frac{C}{C_0}\left[1 - \left(\frac{C}{C_0} \right) \right] \right\} C_0 \tag{4}$$

where "C" corresponds to the dye concentration in time, C_0 to the initial dye concentration, and "k" is the variation rate at the inflection point, thus corresponding to the kinetic constant. For parameter "k", a linear model was fitted as a function of current density "j" (A·m^{-2}), obtaining an R^2 of 0.9959. The model for the value of "k" as a function of "j" is presented in Eq. (5):

$$k = 0.0042 j + 0.01195 \tag{5}$$

2.2.3. Boundary conditions

For fluid flow, boundary conditions of the inlet, outlet, slip at the free surface, and no-slip at the wall were employed, as described in Table 1 [61]. The reference pressure of the outlet was atmospheric. Boundary conditions for mass transfer are also described in Table 1 and include flow, outflow, and no flux at the walls.

Table 1
Boundary conditions applied to the simulations

Physics	Boundary condition	Equation[a]	
Fluid flow	Inlet	$\boldsymbol{u} = -U_0 \boldsymbol{n}$	(6)
	Outlet	$\left[-p\boldsymbol{I} + \mu\left(\nabla\boldsymbol{u} + \left(\nabla\boldsymbol{u} \right)^T \right) \right]\boldsymbol{n} = -\hat{p}_0\,\boldsymbol{n}$	(7)
		$\hat{p}_0 \le p_0$	(8)
	No slip	$\boldsymbol{u} = 0$	(9)
	Slip	$\boldsymbol{u} \cdot \boldsymbol{n} = 0$	(10)
		$\left[-p\boldsymbol{I} + \mu\left(\nabla\boldsymbol{u} + \left(\nabla\boldsymbol{u} \right)^T \right) \right]\boldsymbol{n} = 0$	(11)
Mass transport	No flux	$-\boldsymbol{n}\left(-D\nabla C + \boldsymbol{u}C \right) = 0$	(12)
	Inflow	$c_i = C_0$	(13)
	Outflow	$-\boldsymbol{n} \cdot D_i \nabla c_i$	(14)
	Reactions	$\nabla \cdot \left(-D_i \nabla c_i \right) + \boldsymbol{u} \cdot \nabla c_i = R_i$	(15)

[a]U_0 = inlet velocity; $\boldsymbol{n}$ = normal direction; c_i = concentration of species i; D_i = diffusivity coefficient of species i.

The relative tolerance adopted for simulations was equal to 0.001. The reaction rate and transport properties for the dye species (i.e., diffusivity coefficient equal to 10^{-9} $m^2 \cdot s^{-1}$) were also defined in the domain. For the reaction rate, the reaction domain size was defined according to the iron distribution in the reactor, as observed in the experiments described in section 2.3.1. To compute the steady-state solution for each test, the iterative solver "Segregated", suggested by the software for the problem, was used.

2.2.4. Mesh convergence study

A mesh convergence study was carried out to determine the best mesh for the simulations, which could guarantee that the solution was not mesh-dependent while avoiding the unnecessary use of computational resources.

The convergence study was performed by running simulations of the electrochemical reactor with the conditions presented in Table 2 with different meshes, progressively more refined, and then comparing their results.

Element size parameters for each simulation were defined using the meshes generated automatically by COMSOL Multiphysics® with the physics-controlled mesh option, which auto-adjusts mesh configurations to promote better refinement in higher gradient areas. Element size was calibrated for CFD, and the element type configuration was defined as "all elements", so the final mesh was composed of tetrahedron, pyramidal, prism, triangular, quadrilateral, and corner elements.

The values for the element size parameters in each simulation are described in Table 3.

For a comparison of simulation and experimental results, a data set was defined corresponding to a line that cut the reactor longitudinally, at half its width (6.5 cm) (chosen because it was the area that presented more significant gradients), and at the same height as the sampling device (6 cm).

Dye concentration results for each mesh as a function of the distance on the "*x*" axis (linear profile) in the data set adopted for analysis are presented in Fig. 3.

Fig. 3 shows how, as the mesh becomes more refined, the predicted maximum concentration between two electrodes increases. Moreover, as the mesh refinement increases, its results get closer to those obtained with the most refined mesh (Normal). The 'Coarse' mesh configuration was adopted as its results were sufficiently close to those predicted with the 'Normal' setting. Fig. 4 shows the chosen mesh.

2.2.5. Simulation conditions

For experimental validation, simulation conditions different than those used to fit the kinetics model in the batch tests were used so that the predictive performance of the full-scale model could be checked under new conditions. They are described in Table 4.

2.3. Experimental procedure

2.3.1. Experimental calibration of boundary conditions

Preliminary experiments were carried out in the continuous reactor to obtain preliminary knowledge of the

Table 2
Conditions of the simulations for the convergence study

Flow rate (L·min⁻¹)	0.5
Inlet velocity (cm·s⁻¹)	1.644
Hydraulic retention time (min)	17
Initial concentration (mg·L⁻¹)	40
Current for each pair of electrodes (A)	1.5
Current density (A·m⁻²)	73.26

Fig. 3. Dye concentration for each mesh.

Table 3
Parameters of elements size for the study of mesh convergence

Parameter	Mesh				
	Extremely coarse	Extra coarse	Coarser	Coarse	Normal
Maximum element size (cm)	3.95	2.39	1.55	1.2	0.801
Minimum element size (cm)	0.837	0.598	0.478	0.359	0.239
Maximum element growth rate (cm)	1.4	1.3	1.25	1.2	1.15
Curvature factor	1	0.9	0.8	0.7	0.6
Resolution of narrow regions	0.3	0.4	0.5	0.6	0.7
Number of elements	83,569	129,801	248,083	537,020	1,254,592

iron dispersion in the reactor, which would be relevant for establishing reaction boundary conditions.

Although the reaction kinetics model does not include iron concentration as an independent variable, the presence of coagulant ions is a prerequisite for the occurrence of the reaction. Moreover, according to Safonyk and Prysiazhniuk [52], analysis of iron distribution inside the reactor allows the prediction of hydrodynamic phenomena, such as internal recirculation and dead zones, which affect the formation of a coagulant. The knowledge of iron ions' dispersion in the reactor is thus critical to determine the point of the reactor in which the reaction begins so that it can be accurately reproduced in the simulations by correctly placing the respective boundary condition and reaction domain size.

Experiments were carried out under four flow conditions to verify whether flow rate could influence the distribution of iron in the reactor. It was assumed that this could happen because of hydrodynamic phenomena, such as vortices
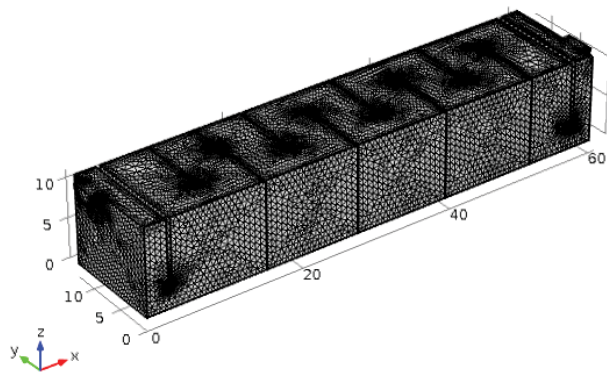

Fig. 4. Mesh adopted for simulations.

and preferential zones. Such phenomena were not included in the hydrodynamic model since, similarly to most of the CFD studies of electrochemical reactors [37], it did not consider the influence of gas microbubbles in the flow. The observation of this phenomenon in experiments was thus deemed crucial to substantiate the decision regarding boundary conditions for the reaction domain since the presence of iron ions assures the beginning of the reaction.

Reactor operation in these tests was the same as described in section 2.1. The experimental test conditions are presented in Table 5.

The distribution of iron in the reactor was carefully observed based on pictures of its steady-state operation. The steady-state regime was ensured by waiting at least twice the hydraulic retention time (in these conditions, a total of 40 min) before taking the pictures.

Fig. 5 shows the steady-state iron distribution for the four tests. The inlet deflector is shown on the left side of the images, so the effluent flows from left to right in the pictures. The effluent entrance point in the reactor is located in the upper left corner, before the deflector [37].

The presence or absence of iron ions between the deflector and the first electrode is the most important aspect for analysis in these images since, theoretically, there should be no coagulating ions in this zone, given that the left surface of the first electrode (cathode) is not active.

In the case of Test I, with a flow rate equal to 0.5 L·min^{-1}, an unexpectedly high iron accumulation between the deflector and the first electrode is observed. This is likely due to bubbles causing hydrodynamic phenomena, such as vortices, to form in the counterflow direction to the effluent flow.

For the 1 L·min^{-1} flow condition, on the other hand, although the backflow of iron was also observed, the amount of species in the counter-flow direction is visibly lower. Note that, for the 0.5 L·min^{-1} condition, a thick iron layer
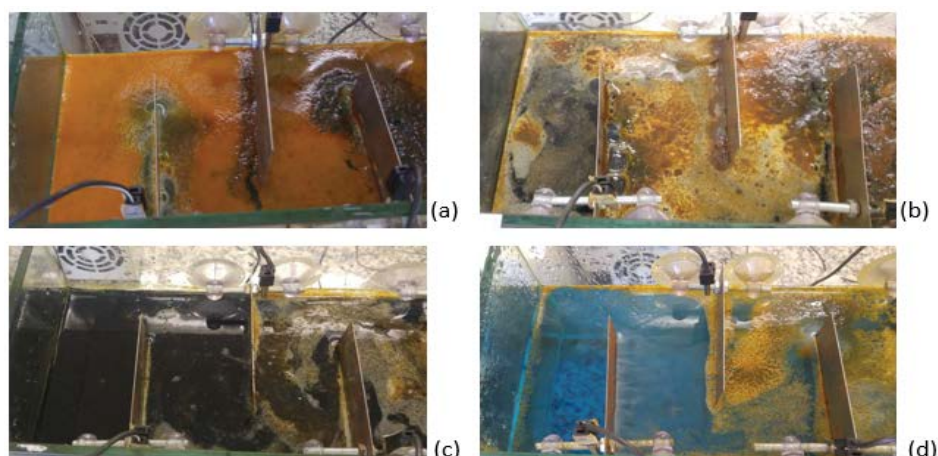
Table 4
Simulation conditions

Test	Flow rate (L·min^{-1})	Inlet velocity, U_0 (cm·s^{-1})	Hydraulic retention time (min)	Initial dye concentration (mg·L^{-1})	Current for each pair of electrodes (A)	Current Density (A·m^{-2})
1	0.5	1.644	17.00	40	1.5	73.26
2	0.5	1.644	17.00	25	1.5	73.26
3	1.0	3.466	8.50	40	1.5	73.26
4	1.5	5.199	5.67	40	1.5	73.26
5	2.0	6.930	4.25	40	1.5	73.26

Table 5
Conditions of the continuous flow experiments for the analysis of the iron distribution in the reactor

Test	Current for each pair of electrodes (A)	Effluent flow rate (L·min^{-1})	Hydraulic retention time (min)	Dye concentration (mg·L^{-1})
I	1.5	0.5	17.00	5
II	1.5	1.0	8.50	25
III	1.5	1.5	5.60	25
IV	1.5	2.0	4.25	5

Fig. 5. Distribution of iron in the reactor, in the steady state, for the flow conditions: (a) 0.5 L·min^{-1}, (b) 1 L·min^{-1}, (c) 1.5 L·min^{-1} and (d) 2 L·min^{-1}.

accumulated in the studied area, while for the 1 L·min^{-1} condition this did not occur, seen as the effluent remains visible in some areas.

As illustrated in the images, iron distribution in the reactor also shows that iron backflow did not happen for conditions of 1.5 and 2 L·min^{-1}. Thus, it is inferred that the higher flow rates reduce the effect of the hydrodynamic phenomena that cause the backflow of iron so that no coagulant ions accumulate in the region before the first electrode.

When investigating the influence of turbulence sources, such as bubbles, on hydrodynamic behavior in electrocoagulation reactors, Colli and Bisang [62] observed that, accordingly, the dispersion coefficient increases with gas generation at low flow rates but that it is not affected at higher flow rates.

Therefore, the starting point of the dye removal reaction differs among the four flow conditions. In Test I, due to a lower flow rate, the reaction starts from the deflector onwards due to iron accumulation. In Test II, since there was no excessive iron accumulation between the deflector and the first electrode, the reaction was assumed to start from the first electrode onwards, according to EC theory. For Tests III and IV, there is a certainty that the reaction starts from the first electrode onwards since there are no coagulant ions before this point.

This information was used to define the boundary conditions for the reaction starting point in simulating the reactor's dye concentration profile.

2.3.2. Experimental validation

Experimental runs with the same conditions as used in the numerical simulations (presented in Table 4) were performed in the experimental module to validate the full-scale model for the concentration profile in the reactor (including physics for fluid dynamics and reaction kinetics). The reactor operation was the same as described in item 2.1. In order to avoid electrode passivation, electrodes were frequently replaced, and electrode polarity was inverted after each test.

The tests were carried out with one repetition, and samples were collected in triplicate after a period of twice the hydraulic retention time (after 40 min). Samples were taken at several points along the reactor, in the longitudinal and transversal directions, at approximately 6 cm of height. The sampling mesh was defined according to preliminary simulations and is shown in Fig. 6.

Samples were left to settle in test tubes for about 12 h. Residual dye concentration in each sample was determined in duplicate by absorbance spectrophotometry in the UV-Vis range (Hach DR 2800), at a wavelength of 618 nm, which was adopted following the recommendations of Santos et al. [29]. Experimental procedures are further detailed in Gasparovic et al. [57].

3. Results and discussion

3.1. Flow field in the reactor

Numerical simulations for the fluid flow in the reactor allow to predict the hydrodynamic behavior in the reactor, both in terms of velocity and direction of flow. The flow velocity profiles obtained with simulations for the two extreme velocity conditions tested (0.5 L·min^{-1} corresponding to Tests 1 and 2, and 2 L·min^{-1} corresponding to Test 5) are shown in Fig. 7, which corresponds to a parallel cut of the "x–y" plane, at the same height chosen for sampling (6 cm). Flow velocity in the reactor is represented by the color scale, and white arrows represent the flow direction at each point. A logarithmic scale for arrow length was used in the images, to allow representation of the flow direction of a more extensive range of velocities. The color scale was also saturated for better visualization. In the images, the flow inlets and outlets in the reactor are located in coordinates (0, 12) and (60, 2), respectively.

The simulations for the two conditions showed flow profiles with a few similar characteristics. Hydrodynamic phenomena expected in electrochemical cells are noticeable, such as a preferential flow zone in the center of the cell, near the electrodes, internal recirculation in some cell zones, and some dead zones [45].
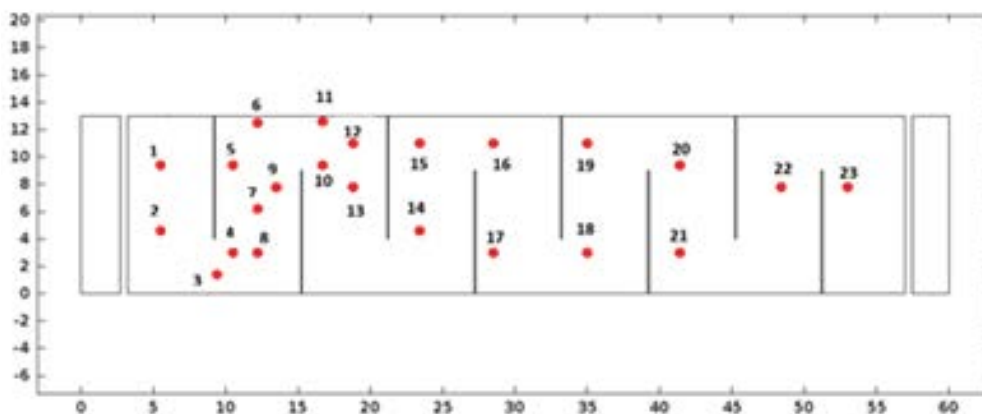
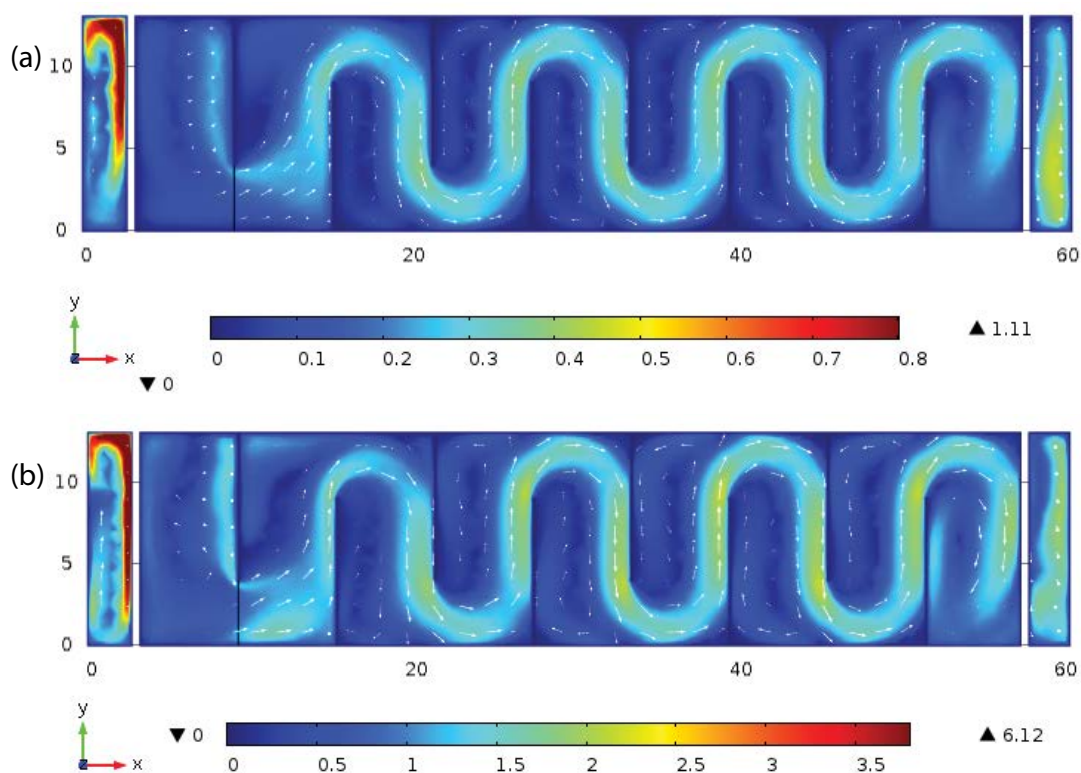Fig. 6. Sample mesh in the continuous flow module.

Fig. 7. Velocity and field velocity for the conditions tested. Velocities (cm·s^{-1}) and velocity field (arrows) for Tests 1 and 2 (flow rate: 0.5 L·min^{-1}) and (b) velocities (cm·s^{-1}) and velocity field (arrows) for Test 5 (flow rate: 2 L·min^{-1}).

The main differences in simulation results between the two conditions refer to velocity magnitude, which is approximately six times higher in Test 5 than in Tests 1 and 2. While for the lower flow rate condition the maximum flow velocity reaches 1.11 cm·s^{-1}, in the one with the highest flow rate the maximum velocity is 6.12 cm·s^{-1}.

According to Safonyk and Prysiazhniuk [52] the flow regime in the electrocoagulation reactor can be either laminar or turbulent. In complex geometry, the speed field includes a random turbulent component that generates streams and turbulent vortices. Given the complex geometry of the present system, it is likely that a random turbulency

element is present, which has yet to be fully captured by the model, which considered laminar flow.

As a consequence, limitations in the hydrodynamic model are possible sources of error. For example, when comparing the simulation with the behavior observed in the tests to determine iron distribution in the reactor, it is noticeable that the phenomena of internal recirculation and vortex formation are underestimated in the model. This is mainly visible near the flow inlet, which has almost no recirculation in the simulation. In contrast, in Test 1, with a lower flow rate, the recirculation in that area is significant enough to cause iron backflow. These considerations will

further inform the discussion of the dye concentration simulations and the experimental validation of the model.

3.2. Dye concentration profile and experimental validation

Numerical results for the dye concentration in the reactor were plotted on a 2D graphic of a 'cut plane' dataset at the height of 6 cm from the reactor base, the same height as the sampling points. Fig. 8 shows the predicted concentration profile (mg·L^{-1}) in simulations for Tests 1–5.

The profiles shown in Fig. 8 illustrate the influence of flow dynamics on treatment efficiency, as predicted by the model. For the operating conditions employed and a flow rate of 0.5 L·s^{-1} (Tests 1 and 2), the model predicts a successful treatment, such that at half of the reactor's length, the predicted concentration is already below 5 mg·L^{-1}. When the flow rate is increased to 1 L·s^{-1} (Test 3), 1.5 L·s^{-1} (Test 4), and 2 L·s^{-1} (Test 5), there is a progressive reduction in the predicted efficiency of the treatment at the same point in the reactor.

The phenomena predicted in the simulation of hydrodynamics, such as the preferential flow zone in the center of the cell, seem to directly influence the simulated concentration profile through insufficient mixture in the area between each pair of electrodes. This is visible in the high concentration gradient observed between the higher and lower velocity areas between the same electrodes. By increasing the flow rate, such gradients are also accentuated. Note that, according to the previous indication of limitations in the hydrodynamic model as possible sources of error, such a gradient would possibly not be observed experimentally.

The concentrations predicted in the simulations were compared to experimental results in tests carried out under the same conditions, as demonstrated in the graph of observed vs. predicted concentration (Fig. 9) and the relative error for dye removal (Table 6). The analysis of these graphs and data, along with the simulated profiles (Fig. 8), allows us to reach a conclusion regarding the model's validity.

For Tests 1 and 2, Fig. 9a and b show how the model could adequately predict the concentration profile throughout the module and the removal efficiency at the exit point, which is essential information for the design of a reactor. For Test 1, the model correctly indicates that from the third electrode on (x = 22.7 cm), the removal rate is greater than 90%.

The model also predicted that from the first electrode onwards, the residual dye concentration would be less than half of the inflow concentration for both tests. This fact confirms the conclusions reached based on the iron dispersion tests in the reactor since, for the flow rate of 0.5 L·s^{-1}, the reaction starting point indeed occurs between the deflector and the first electrode.

Only for the second point (x = 5.5 cm) of Test 2 a more significant error was observed, possibly due to the model's limitations regarding hydrodynamics. Thus, for Tests 1 and 2, the reactor's concentration profile and the number of electrodes required for the treatment were well represented, presenting a relative error of removal at the reactor exit in the order of 2%.

For Test 3, in general, the model successfully predicted the removal efficiency in the entrance and exit areas of the

reactor while differing significantly from experiments in the intermediate regions. This is likely due to the influence of the dead zones incorrectly predicted by the model. As the mixture in the experimental reactor is better than predicted by the model, the concentration gradient between each pair of electrodes is smaller than simulated. Regarding treatment efficiency, however, the model accurately predicted dye concentrations at the points located in the exit region (points 21, 22, and 23), with a relative error for dye removal of less than 1% for the last sampling point, correctly anticipating that the dye concentration remaining in the effluent after the treatment is about 5 mg·L^{-1}.

As a whole, the model was able to predict the dye decay profile throughout the module, and interestingly for this test, a curve of sigmoidal characteristics was observed. Therefore, for this flow rate condition, the model was also considered valid, as it provided the most critical information for reactor sizing and design: the removal efficiency at the exit of the reactor.

Tests 4 and 5 were performed with the highest flow rates, equal to 1.5 and 2 L·min^{-1}, respectively. It had been assumed that the reaction would not occur before the first electrode, which was confirmed by the experimental data presented in Fig. 9d and e.

The performances of both tests were similar and will be discussed together. In both, the model error for the initial values was lower than 2 mg·L^{-1}; however, from the half-point (length-wise) of the reactor on, the error was higher than for other tests, greater than 20 mg·L^{-1} for several sampling points. At the reactor exit, the relative error for removal was 24.2% and 56.5% for Tests 4 and 5, respectively. Hence for these flow rate conditions, the model was not considered valid. However, it did provide relevant information, accurately predicting that the dye removal in the initial part of the module is negligible.

Possible experimental errors aside, this can be explained by the module being undersized for a complete treatment. Consequently, concentrations remain high throughout the reactor, amplifying the model's failure to fully capture the mixture between each pair of electrodes. This is visible in the difference between concentration in the dead zones and the preferential flow route. With the improvement in mixture due to bubble mixing that is observed experimentally, the concentration in these regions becomes more homogeneous.

As a matter of fact, most of the sampling points from the second electrode onward are in dead zones. If sampling had been conducted in the preferential flow route, which presents better homogenization and where the simulation concentrations are higher and closer to the experimental values, the difference between numerical and experimental concentrations would likely have been lower. At sampling points 15 and 22, for example, which have among the highest error, a change of a few centimeters would raise the predicted concentration to 10 mg·L^{-1}, a difference of the same order of magnitude as the error.

The exit region is especially relevant because it indicates treatment efficiency. Sampling point 23 also happens to be located in one of the simulated dead zones, in which the higher (simulated) retention time leads to a lower final concentration. Meanwhile, concentrations much closer to
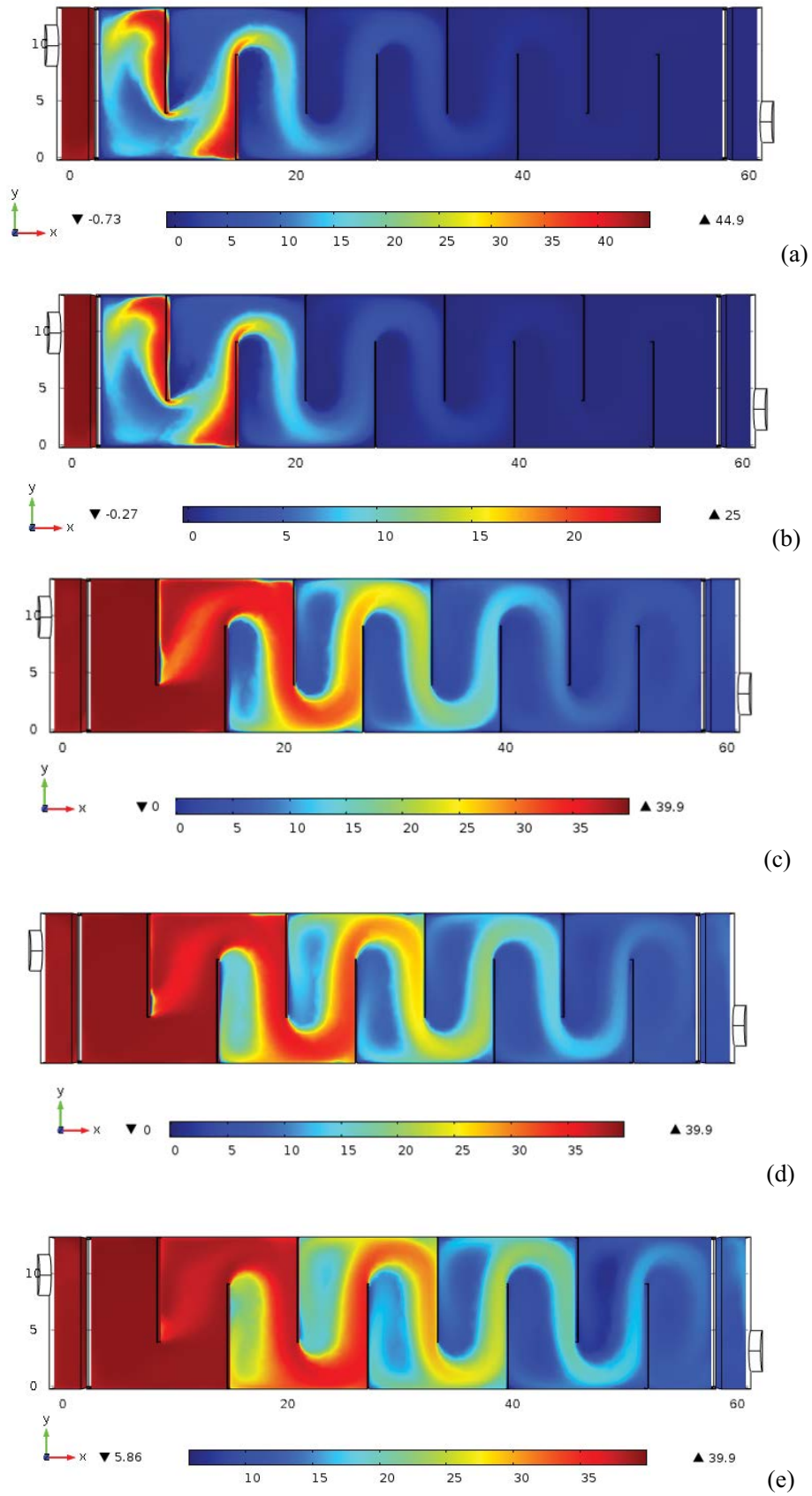
Fig. 8. Simulated concentration profile for tests (a) 1, (b) 2, (c) 3, (d) 4 and (e) 5.
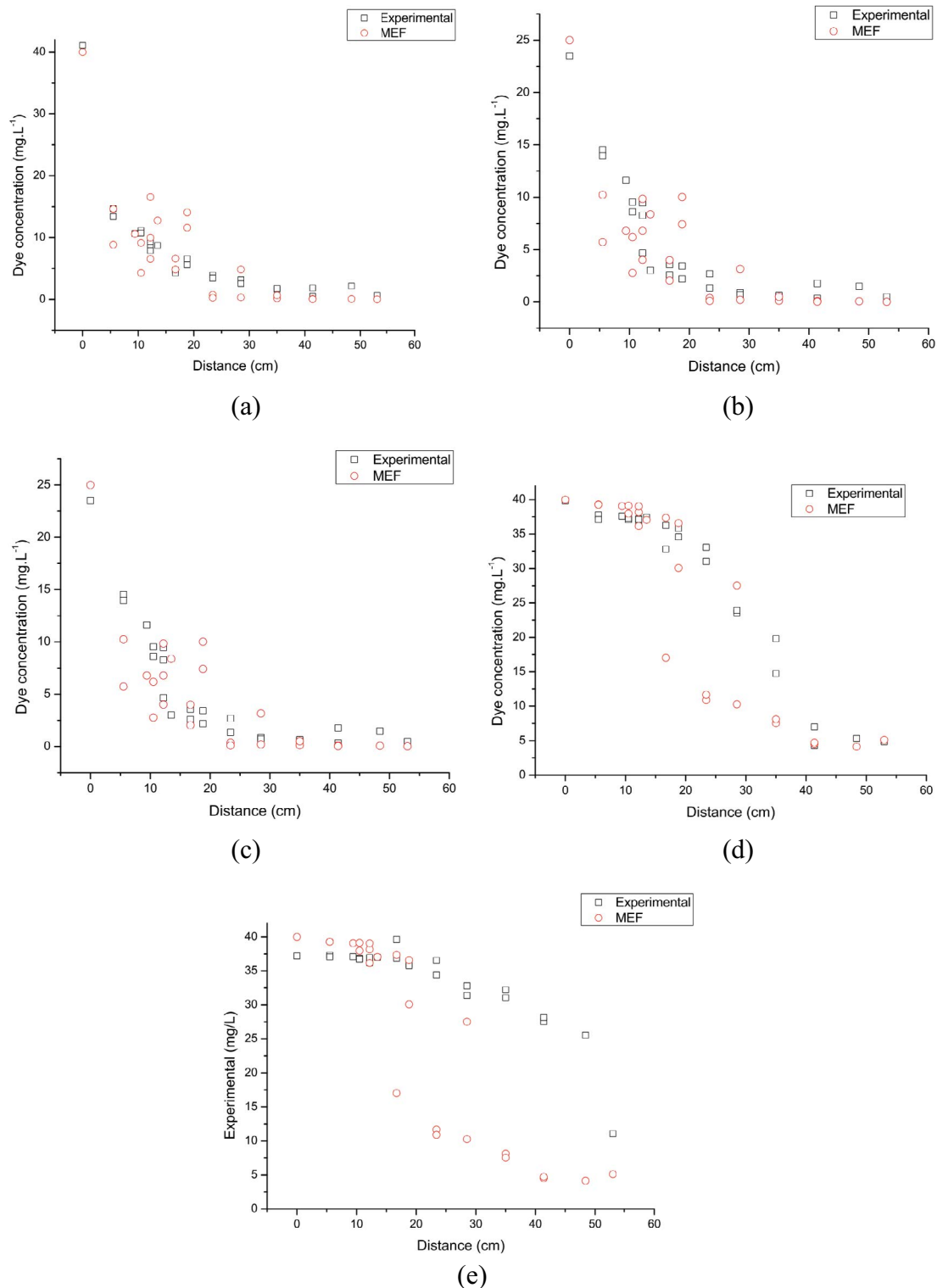
Fig. 9. Predicted and observed values for dye concentration and Tests 1–5.

the experimental value can be found in the simulation in areas closer to the deflector.

Another possible source of error, unique to these two Tests (4 and 5), is the influence of flow rate on iron distribution in the reactor. In Tests 1 and 2 (flow rate of 0.5 L·min⁻¹),

a thick layer of iron was observed from the deflector, guaranteeing that the reaction started at that point. In the case of Tests 4 and 5, similar characteristics were observed only from the third pair of electrodes on. It is then possible that iron concentrations prior to that point are insufficient for

Table 6
Relative error for dye removal (–)

Distance (cm)	Test 1	Test 2	Test 3	Test 4	Test 5
0	0.000	0.000	0.000	0.000	0.000
5.5	0.014	0.547	0.667	4.386	3.513
5.5	0.157	0.898	0.733	4.820	37.587
9.4	0.008	0.444	0.584	10.37	6.478
10.5	0.044	0.188	0.678	3.925	2.563
10.5	0.226	0.496	0.210	0.803	1.748
12.2	0.061	0.047	0.475	0.678	0.854
12.2	0.029	0.218	0.456	11.67	3.268
12.2	0.275	0.065	0.642	2.928	0.884
13.5	0.135	0.238	0.222	12.312	1.940
16.7	0.019	0.032	2.259	6.414	24.109
16.7	0.057	0.011	0.261	7.826	0.251
18.8	0.155	0.176	0.146	1.466	1.767
18.8	0.249	0.339	0.888	5.354	4.997
23.4	0.085	0.056	2.292	8.391	14.006
23.4	0.084	0.112	3.158	39.395	9.719
28.5	0.048	0.092	0.237	1.648	4.249
28.5	0.058	0.022	0.858	3.749	3.192
35	0.028	0.007	0.615	3.828	7.192
35	0.037	0.021	0.266	5.071	5.069
41.4	0.045	0.011	0.076	2.425	5.324
41.4	0.011	0.080	0.011	2.621	2.782
48.4	0.054	0.065	0.035	1.868	5.285
53	0.016	0.019	0.007	0.242	0.565

the reaction to take place and that dye removal actually starts further on than the boundary condition adopted in the simulation. Therefore, how the flow influences iron distribution along the reactor, the minimum iron concentration required for the reaction to occur, and the effect of these phenomena in the electrocoagulation reaction are all aspects that greatly influence treatment efficiency in continuous reactors and are, however, little discussed in scientific literature.

In all, the model for dye concentration profile in the reactor, which encompasses reaction kinetics as well as fluid dynamics and transport models, and when used in finite element method simulations with its current limitations, was proven valid for the conditions of Tests 1, 2 and 3, and not for the ones on Tests 4 and 5. Therefore, the model is valid to predict the concentration profile in the reactor within a working range for the following variables: flow rate 0.5–1 L·min⁻¹, and HRT 8.5–17 min.

3.3. Treatment efficiency

Having performed the experimental validation of the model, experimental results for dye concentration at the reactor exit are analyzed to assess the system's removal efficiency and how it compares to results found in the literature. These results and information on the dye type and reactor for each study are presented in Table 6. Results from this work are highlighted.

As expected from the concentration profiles, the dye removal efficiency of the continuous reactor decreases as the flow rate increases. For rates up until 1 L·min⁻¹ (that is, the same range for which the model was considered valid),

Table 6
Experimental removal efficiencies from literature and this study

References	Dye and concentration	Electrode material, area, and current density	Type of reactor, volume, or flow rate	Removal efficiency
Nandi and Patel [27]	Bright Green 42040, 100 mg·L⁻¹	Fe, 72 cm², 13.9–138.9 A·m⁻², 1–3 cm	Batch, 1 L	99.59%
Amani-Ghadim et al. [24]	Reactive Red 43, 50 mg·L⁻¹	Al or Fe (anode), stainless steel (cathode), 5 cm²*, 10.86–39.14 A·m⁻², 20 mm	Batch, 1.8 L	>99%
Pajootan et al. [28]	Acid Black 52, Acid Yellow 220, 200 mg·L⁻¹	Al, 10 cm²*, 10–120 A·m⁻², 10 mm	Batch, 250 mL	85.68% (B52); 93.41% (Y220)
Zodi et al. [30]	Direct Red 81, 50 mg·L⁻¹	Al, 200 A·m⁻², 10 mm	Continuous, 10–28 L·h⁻¹	90.2% (10 L·h⁻¹); 76.8% (28 L·h⁻¹)
Merzouk et al. [63]	Red dye, up to 200 mg·L⁻¹	Al, 48 cm², 31.25 mA·cm⁻², 1 cm	Continuous, 8.6 L, 25–78 L·h⁻¹, MP-P	>85%
Phalakornkule et al. [2]	Reactive Blue 140, 100 mg·L⁻¹	Fe or Al, 1,047 cm², 10–40 m A·m⁻², 5–12 mm	Batch, 1.8 L	>95%
Aoudj et al. [64]	Direct Red 81, 50 mg·L⁻¹	Al, 40 cm², 0.125–5 mA·cm⁻², 0–5 cm	Batch, 500 mL	>98%
Santos et al. [29]	Reactive Blue 5G, 50 mg·L⁻¹	Fe, 25 cm², 4–60 mA·cm⁻², 1 cm	Batch, 500 mL	86.77%
This work	Reactive Blue 5G, 25–40 mg·L⁻¹	Fe, 99 cm², 73.26 A·m⁻²	Continuous, 8.5 L, 0.5–2 L·min⁻¹	Test (1) 98%; (2) 98%; (3) 88%; (4) 70%; (5) 48%

efficiency results are well within the range found in the literature. For flow rates above this threshold, efficiency is significantly lower, and the reactor would be considered undersized for most purposes.

Nevertheless, results show that when reactor size and flow rate are adequately matched, the reactor performs similarly to the best results found in the literature. This confirms that within the valid range of flow rates, the novel modelling approach suggested in this paper can be used for the design of EC reactors.

4. Conclusions

This work contributes to the literature gap regarding the modeling and simulation of electrocoagulation reactors for wastewater treatment. This paper sheds light on overcoming a significant obstacle to the consolidation of this technology, namely, the need for a systematic methodology for the design of reactors.

A new modeling approach is introduced, which couples computational fluid dynamics to an experimentally fitted kinetic model for pollutant removal. It addresses and predicts the efficiency of electrocoagulation treatment by computing the concentration profile in the reactor for different operating conditions. The simulations demanded reasonably small computational resources, one of the limitations pointed out in the literature, with no significant loss of information.

The proposed model was shown to be valid for a range of flow rates and HRT, from 0.5 to 1 L·min^{-1} and 8.5 to 17 min, respectively. Despite model limitations for not including some of the phenomena involved in electrocoagulation, such as electrochemistry and the influence of pH and bubbles, the simulated profiles were reasonably close to experimental results. Numerical and experimental results also shed light on the influence of hydrodynamics in the iron distribution along the reactor and its effect in the reaction domain. In addition, the model provided information that would be essential for designing and determining reactor operating conditions.

In conclusion, this methodology contributes to overcoming known and relevant obstacles in the design of electrocoagulation reactors, thus providing means to consolidate this promising technology for wastewater treatment. The model can be developed further by considering turbulent flow and phenomena such as bubbles, modeling the electrochemistry processes, and calculating current efficiency, energy consumption, and costs.

Symbols

C	—	Dye concentration, mol·m^{-3}
C_0	—	Initial concentration of dye in effluent, mol·m^{-3}
c_i	—	Concentration of species i, mol·m^{-3}
D_i	—	Diffusivity coefficient of species i, m^2·s^{-1}
g	—	Gravity field, m·s^{-2}
I	—	Identity matrix
j	—	Current density, A·m^{-2}
k	—	Kinetic constant for dye removal, s^{-1}
n	—	Normal vector

p	—	Fluid pressure, Pa
p_0	—	Reference pressure, Pa
R_i	—	Reaction rate for dye removal, mol·m^{-3}·s^{-1}
T	—	Matrix transpose operator
u	—	Velocity field, m·s^{-1}
U_0	—	Inlet velocity, m·s^{-1}

Greek

μ	—	Fluid viscosity, Pa·s
ρ	—	Specific mass, kg·m^{-3}

Subscripts

0	—	Initial conditions
i	—	Species i

Declarations of interest

None.

References

[1] L. Chen, L. Wang, X. Wu, X. Ding, A process-level water conservation and pollution control performance evaluation tool of cleaner production technology in textile industry, J. Cleaner Prod., 143 (2017) 1137–1143.

[2] C. Phalakornkule, S. Polgumhang, W. Tongdaung, Electrocoagulation of blue reactive, red disperse and mixed dyes, and application in treating textile effluent, J. Environ. Manage., 91 (2010) 918–926.

[3] G.T. Güyer, K. Nadeem, N. Dizge, Recycling of pad-batch washing textile wastewater through advanced oxidation processes and its reusability assessment for Turkish textile industry, J. Cleaner Prod., 139 (2016) 488–494.

[4] I. Pillai, M. Sasidharan, A.K. Gupta, Performance analysis of a continuous serpentine flow reactor for electrochemical oxidation of synthetic and real textile wastewater: energy consumption, mass transfer coefficient and economic analysis, J. Environ. Manage., 193 (2017) 524–531.

[5] K. Hasani, M. Moradi, SA. Mokhtari, H. Sadeghi, A. Dargahi, M. Vosoughi, Degradation of Basic Violet 16 dye by electroactivated persulfate process from aqueous solutions and toxicity assessment using microorganisms: determination of by-products, reaction kinetic and optimization using Box–Behnken design, Int. J. Chem. React., 19 (2021) 261–275.

[6] M.R. Samarghandi, A. Dargahi, H. Zolghadr Nasab, E. Ghahramani, S. Salehi, Degradation of azo dye Acid Red 14 (AR14) from aqueous solution using H$_2$O$_2$/nZVI and

$S_2O_8^{2-}$/nZVI processes in the presence of UV irradiation, Water Environ. Res., 92 (2020) 1173–1183.

[7] A. Bafana, S.S. Devi, T. Chakrabarti, Azo dyes: past, present and the future, Environ. Rev., 19 (2011) 350–370.

[8] V. Khandegar, A.K. Saroha, Electrochemical treatment of textile effluent containing Acid Red 131 dye, J. Hazard. Toxic Radioact. Waste, 18 (2014) 38–44.

[9] C.D. Raman, S. Kanmani, Textile dye degradation using nano zero valent iron: a review, J. Environ. Manage., 177 (2016) 341–355.

[10] F.M.M. Paschoal, G. Tremiliosi-Filho, Aplicação da tecnologia de eletrofloculação na recuperação do corante índigo blue a partir de efluentes industriais, Quim. Nova, 28 (2005) 766–772.

[11] A. Cerqueira, C. Russo, M.R.C. Marques, Electrofloculation for textile wastewater treatment, Braz. J. Chem. Eng., 26 (2009) 659–668.

[12] A.N. Módenes, F.R. Espinoza-Quiñones, D.R. Manenti, F.H. Borba, S.M. Palácio, A. Colombo, Performance evaluation of a photo-Fenton process applied to pollutant removal from textile effluents in a batch system, J. Environ. Manage., 104 (2012) 1–8.

[13] R. Lambretch, Adsorption of the dye Reactive Blue 5G in retorted shale, Braz. J. Chem. Eng., 32 (2015) 269–281.

[14] V. Katheresan, J. Kansedo, S.Y. Lau, Efficiency of various recent wastewater dye removal methods: a review, J. Environ. Chem. Eng., 6 (2018) 4676–4697.

[15] A. Kunz, P. Peralta-zamora, Novas tendências no tratamento de efluentes têxteis, Quím. Nova, 25 (2002) 78–82.

[16] M.F. Klen, Adsorption kinetics of Blue 5G dye from aqueous solution on dead floating aquatic macrophyte: effect of pH, temperature, and pretreatment, Water Air Soil Pollut., 223 (2012) 4369–4381.

[17] A. Peyghami, A. Moharrami, Y. Rashtbari, S. Afshin, M. Vosuoghi, A. Dargahi, Evaluation of the efficiency of magnetized clinoptilolite zeolite with Fe_3O_4 nanoparticles on the removal of Basic Violet 16 (BV16) dye from aqueous solutions, J. Dispersion Sci. Technol., 44 (2021) 278–287.

[18] O.T. Can, M. Bayramoglu, M. Kobya, Decolorization of reactive dye solutions by electrocoagulation using aluminum electrodes, Ind. Eng. Chem. Res., 2 (2003) 3391–3396.

[19] P. Jegathambal, A. Gafoor, Two-stage hybrid electrocoagulation–adsorption in the removal of disperse dyes and inorganic salts from the textile dyeing effluent, Desal. Water Treat., 237 (2021) 27685, doi: 10.5004/dwt.2021.27685.

[20] M. Rahmanihanzaki, A. Hemmati, A review of mineral carbonation by alkaline solid waste, Int. J. Greenhouse Gas Control, 121 (2022) 103798, doi: 10.1016/j.ijggc.2022.103798.

[21] D. Ghernaout, M.W. Naceur, B. Ghernaout, A review of electrocoagulation as a promising coagulation process for improved organic and inorganic matters removal by electrophoresis and electroflotation, Desal. Water Treat., 28 (2011) 287–320.

[22] B. Merzouk, K. Madani, A. Sekki, Using electrocoagulation–electroflotation technology to treat synthetic solution and textile wastewater, two case studies, Desalination, 250 (2010) 573–577.

[23] A. Akhtar, Z. Aslam, A. Asghar, M.M. Bello, A.A.A. Raman, Electrocoagulation of Congo Red dye-containing wastewater: optimization of operational parameters and process mechanism, J. Environ. Chem. Eng., 8 (2020) 104055, doi: 10.1016/j.jece.2020.104055.

[24] A.R. Amani-ghadim, S. Aber, A. Olad, H. Ashassi-sorkhabi, Optimization of electrocoagulation process for removal of an azo dye using response surface methodology and investigation on the occurrence of destructive side reactions, Chem. Eng. Process. Process Intensif., 64 (2013) 68–78.

[25] A.S. Assémian, K.E. Kouassi, A.E. Zogbé, K. Adouby, P. Drogui, *In-situ* generation of effective coagulant to treat textile bio-refractory wastewater: optimization through response surface methodology, J. Environ. Chem. Eng., 6 (2018) 5587–5594.

[26] N.S. Houssini, A. Essadki, E. Elqars, Removal of Reactive Blue and disperse red dyes from synthetic textile effluent by electrocoagulation process using Al-Al and Fe-Fe electrodes:

[27] B.K. Nandi, S. Patel, Effects of operational parameters on the removal of brilliant green dye from aqueous solutions by electrocoagulation, Arabian J. Chem., 10 (2017) S2961–S2968.

[28] E. Pajootan, M. Arami, N. Mohammad, Binary system dye removal by electrocoagulation from synthetic and real colored wastewaters, J. Taiwan Inst. Chem. Eng., 43 (2012) 282–290.

[29] B.S. Santos, E. Eyng, P.R.S. Bittencourt, L.M. Frare, E.L. Flores, M.B. Costa, Electro-flocculation associated with the extract of *Moringa oleifera* Lam as natural coagulant for the removal of Reactive Blue 5G dye, Acta Sci. Technol., 38 (2016) 438–444.

[30] S. Zodi, B. Merzouk, O. Potier, F. Lapicque, J. Leclerc, Direct Red 81 dye removal by a continuous flow electrocoagulation/flotation reactor, Sep. Purif. Technol., 108 (2013) 215–222.

[31] S. Singh, V.C. Srivastava, I.D. Mall, Mechanistic study of electrochemical treatment of Basic Green 4 dye with aluminum electrodes through zeta potential, TOC, COD and color measurements, and characterization of residues, RSC Adv., 3 (2013) 16426–15439.

[32] A. Doggaz, A. Attour, M. le Page Mostefa, M. Tlili, F. Lapicque, Iron removal from waters by electrocoagulation: investigations of the various physicochemical phenomena involved, Sep. Purif. Technol., 203 (2018) 217–225.

[33] J. Silva, N. Graça, A. Ribeiro, A. Rodrigues, A, Electrocoagulation process for the removal of co-existing fluoride, arsenic and iron from contaminated drinking water, Sep. Purif. Technol., 197 (2018) 237–243.

[34] M.Y.A. Mollah, R. Schennach, J.R. Parga, D.L. Cocke, Electrocoagulation (EC) — science and applications, J. Hazard. Mater., B, 84 (2001) 29–41.

[35] K.S. Hashim, A. Shaw, R. AlKhaddar, P. Kot, A. Al-Shamma'a, Water purification from metal ions in the presence of organic matter using electromagnetic radiation-assisted treatment, J. Cleaner Prod., 280 (2021) 124427, doi: 10.1016/j.jclepro.2020.124427.

[36] W. Bouguerra, K. Brahmi, E. Elaloui, M. Loungou, Optimization of electrocoagulation operating parameters and reactor design for zinc removal: application to industrial Tunisian wastewater, Desal. Water Treat., 56 (2015) 2706–2714.

[37] J.N. Hakizimana, B. Gourich, M. Chafi, Y. Stiriba, C. Vial, P. Drogui, J. Naja, Electrocoagulation process in water treatment: a review of electrocoagulation modeling approaches, Desalination, 404 (2017) 1–21.

[38] P.K. Holt, G.W. Barton, C.A. Mitchell, The future for electrocoagulation as a localised water treatment technology, Chemosphere, 59 (2007) 355–367.

[39] P. Cañizares, F. Martínez, M.A. Rodrigo, C. Jiménez, C. Sáez, J. Lobato, Modelling of wastewater electrocoagulation processes. Part I. General description and application to kaolin-polluted wastewaters, Sep. Purif. Technol., 60 (2008) 155–161.

[40] A.I. Adeogun, R.B. Balakrishnan, Kinetics, isothermal and thermodynamics studies of electrocoagulation removal of basic dye Rhodamine B from aqueous solution using steel electrodes, Appl. Water Sci., 7 (2017), doi: 10.1007/s13201-015-0337-4.

[41] K.P. de Amorim, L.L. Romualdo, L.S. Andrade, Electrochemical degradation of sulfamethoxazole and trimethoprim at boron-doped diamond electrode: performance, kinetics and reaction pathway, Sep. Purif. Technol., 120 (2013) 319–327.

[42] M.R. Majdi, I. Danaee, S. Nikmanesh, Kinetic and thermodynamic investigations on the electrocoagulation of methyl orange from aqueous solution using aluminum electrodes, Bulg. Chem. Commun., 48 (2016) 628–635.

[43] K.L. Dubrawski, C. Du, M. Mohseni, General potential-current model and validation for electrocoagulation, Electrochim. Acta, 129 (2014) 187–195.

[44] A. Vázquez, J.L. Nava, R. Cruz, I. Lázaro, I. Rodríguez, The importance of current distribution and cell hydrodynamic analysis for the design of electrocoagulation reactors, J. Chem. Technol. Biotechnol., 89 (2013) 220–229.

[45] A.I. Vázquez, F.J. Almazán, M.C. Díaz, J.A. Delgadillo, M.I. Lázaro, C. Ojeda, I. Rodríguez, Characterization of a multiple-channel electrochemical cell by computational fluid dynamics (CFD) and residence time distribution (RTD), ECS Trans., 29 (2010) 215–233.

[46] D. Ghernaout, N. Elboughdiri, An insight in electrocoagulation process through current density distribution (CDD), Open Access Lib. J., 7 (2020) 1–12, doi: 10.4236/oalib.1106142.

[47] T. Höhne, V.F. Asl, L.O. Villacorte, M. Herskind, M. Momeni, D. Al-Fayyad, S. Taş-Köhler, A. Lerch, Numerical investigation of degasification in an electrocoagulation reactor, Water (Switzerland), 13 (2021), doi: 10.3390/w13192607.

[48] P. Xiang, Y. Wan, X. Wang, H. Lian, Numerical simulation and experimental study of electrocoagulation grid flocculation tank, Water Sci. Technol., 78 (2018) 786–794.

[49] M. Acil, M. Chafi, B. Gourich, Y. Stiriba, C. Vial, Modeling and Simulation by CFD of an Electrocoagulation Reactor, 12th International Conference on Gas-Liquid & Gas-Liquid-Solid Reactor Engineering, AIChe (American Institute of Chemical Engineers) CEI (Center for Energy Initiatives), New York, NY, U.S.A., 2015.

[50] H.S. Al-Barakat, F.K. Matloub, S.K. Ajjam, T.A. Al-Hattab, Modeling and simulation of wastewater electrocoagulation reactor, IOP Conf. Ser.: Mater. Sci. Eng., 871 (2020) 012002, doi: 10.1088/1757-899X/871/1/012002.

[51] L. Huang, D. Li, J. Liu, L. Yang, C. Dai, N. Ren, Y. Feng, CFD simulation of mass transfer in electrochemical reactor with mesh cathode for higher phenol degradation, Chemosphere, 262 (2021) 127626, doi: 10.1016/j.chemosphere.2020.127626.

[52] A. Safonyk, O. Prysiazhniuk, Modeling of the electrocoagulation processes in nonisothermal conditions, Model. Simul. Eng., 2019 (2019), doi: 10.1155/2019/9629643.

[53] P. Song, Q. Song, Z. Yang, G. Zeng, H. Xu, X. Li, W. Xiong, Numerical simulation and exploration of electrocoagulation process for arsenic and antimony removal: electric field, flow field, and mass transfer studies, J. Environ. Manage., 228 (2018) 336–345.

[54] J. Su, H.Y. Lu, H. Xu, J.R. Sun, J.L. Han, H.B. Lin, Mass transfer enhancement for mesh electrode in a tubular electrochemical reactor using experimental and numerical simulation method, Russ. J. Electrochem., 47 (2011) 1293–1298.

[55] A.H. Hawari, A.M. Alkhatib, M. Hafiz, P. Das, A novel electrocoagulation electrode configuration for the removal of total organic carbon from primary treated municipal wastewater, Environ. Sci. Pollut. Res., 27 (2020) 23888–23898.

[56] A.I. Adeogun, R.B. Balakrishnan, Kinetics, isothermal and thermodynamics studies of electrocoagulation removal of basic dye Rhodamine B from aqueous solution using steel electrodes, Appl. Water Sci., 7 (2017) 1711–1723.

[57] C.L.M. Gasparovic, E. Eyng, L.M. Frare, F. Orssatto, L.B.C. Sabbi, I.J. Baraldi, Kinetics modeling and experimental validation of Reactive Blue 5G dye removal from synthetic solution by electrocoagulation, Desal. Water Treat., 165 (2019) 24331, doi: 10.5004/dwt.2019.24331.

[58] D.T. Moussa, M.H. El-naas, M. Nasser, M.J. Al-marri, A comprehensive review of electrocoagulation for water treatment: potentials and challenges, J. Environ. Manage., 186 (2017) 24–41.

[59] F.M. White, Fluid Mechanics, 8th ed., McGraw-Hill Education, New York, 2016.

[60] M. Carrillo, J.M. González, A New Approach to Modelling Sigmoidal Curves, Universidad de La Laguna, Tenerife, Canary Islands, Spain, 2002.

[61] COMSOL Multiphysics® v. 5.4 COMSOL AB, CFD Module User's Guide, Stockholm, 2018. Available at: www.comsol.com/blogs

[62] A.N. Colli, J.M. Bisang, Evaluation of the hydrodynamic behavior of turbulence promoters in parallel plate electeochemical reactors by means of the dispersion model, Electrochim. Acta, 56 (2011) 7312–7318.

[63] B. Merzouk, B. Gourich, K. Madani, C. Vial, A. Sekki, Removal of a disperse red dye from synthetic wastewater by chemical coagulation and continuous electrocoagulation. A comparative study, Desalination, 272 (2011) 246–253.

[64] S. Aoudj, A. Khelifa, N. Drouiche, M. Hecini, H. Hamitouche, Electrocoagulation process applied to wastewater containing dyes from textile industry, Chem. Eng. Process. Process Intensif., 49 (2010) 1176–1182.